Bacterial motility patterns adapt smoothly in response to spatial confinement and disorder

Haibei Zhang*[1], Miles T. Wetherington*[2,3], Hungtang Ko[4], Cody E. FitzGerald[5], Edwin M. Munro[6] and Jasmine A. Nirody[7]

[1]Graduate Program in Biophysical Sciences, University of Chicago, 929 East 57th St, Chicago, IL 60637
[2]School of Physics, Georgia Institute of Technology, 837 State St NW, Atlanta, GA 30332
[3]School of Applied and Engineering Physics, Cornell University, Clark Hall, 271, 142 Sciences Dr, Ithaca, NY 14853
[4]Department of Mechanical and Aerospace Engineering, Princeton University, 41 Olden St, Princeton, NJ 08544
[5]Department of Engineering Sciences and Applied Mathematics, Northwestern University, 404 2145 Sheridan Rd, Evanston, IL 60208
[6]Department of Molecular Genetics and Cell Biology, University of Chicago, 920 E. 58th St, Chicago, IL 60637
[7]Department of Organismal Biology and Anatomy, University of Chicago, 1027 E 57th St, 407 Chicago, IL 60637

Abstract

Recent studies have shown that *Escherichia coli* in highly confined porous media exhibit extended periods of 'trapping' punctuated by forward 'hops', a significant restructuring of the classical run-and-tumble model of motility. However, bacterial species must navigate a diverse range of complex habitats, such as biological tissues, soil, and sediments. These natural environments display varying levels of both (1) packing density (i.e., confinement) and (2) packing structure (i.e., disorder). Here, we introduce a microfluidic device that enables precise tuning of these environmental parameters, allowing for a more systematic exploration of bacterial motility bridging the extremes of unconfined and highly confined conditions. We observe that motility patterns characteristic of both hop-and-trap and run-and-tumble models coexist in nearly all environments tested, with ensemble dynamics transitioning between these behaviors as both confinement and disorder increase. We demonstrate that dynamics expected from the hop-and-trap model emerge naturally from a modified run-and-tumble model under specific environmental constraints. Our results suggest that bacterial motility patterns lie along a continuum, rather than being confined to a small set of discrete locomotive modes.

Keywords: Bacterial motility, *E. coli*, complex environments, microbial active matter, microfluidics

Introduction

Peritrichously flagellated bacteria like *E. coli*, which have flagellar filaments uniformly distributed around the cell bodies, swim though free solution using 'run-and-tumble' motility [1, 2]. Briefly, the flagellar filaments of a cell form a rotating bundle to propel itself forward during ballistic 'runs'. These periods of directed movement are punctuated by short 'tumbles', during which the flagellar bundle comes apart and the bacterium randomly reorients itself. Recent studies examined how bacterial motility patterns are modified in highly confined environments, reporting that bacteria within tightly packed 3D hydrogels (with average pore size < 4 μm) remained 'trapped' for long periods until they were able to reorient

*These authors contributed equally to this work.

themselves successfully to 'hop' through an opening between pores [3, 4]. Both short- and long-timescale dynamics observed under this 'hop-and-trap' model challenged the longstanding assumption that bacteria would still exhibit run-and-tumble motility in structured environments, only with shorter runs due to collisions with obstacles [5, 6, 7].

Characterizing bacterial motility through structured media is an exciting endeavor because of its relevance to numerous natural and engineered processes including pathogenicity, bioremediation, biomineralization, and drug delivery [8, 9, 10, 11, 12, 13]. However, natural environments contain both densely and sparsely spaced obstacles (e.g., tightly- and loosely-packed soil) arranged in a variety of ordered and disordered patterns (e.g., mucins in different mucosal tissues [14] and various structural patterns found in subsurface layers [15]). Therefore, a comprehensive understanding of bacterial locomotion requires bridging the gap between the extremes of free solution and tightly packed porous media.

Here, we design a microfluidic device to characterize *E. coli* motility in environments with varying levels of confinement and disorder (Fig. 1). We find that bacterial trajectories consistent with both run-and-tumble and hop-and-trap behavior coexist in nearly all structured regions considered. Ensemble dynamics show a gradual transition from those characteristic of run-and-tumble in unconfined media to those more characteristic of hop-and-trap in the most confined environments tested.

Our results suggest that bacterial motility patterns cannot be characterized by a small set of discrete locomotive modes but rather exist along a continuum. We hypothesize that transitions along this continuum depend on the duration of straight swimming periods ('runs' or 'hops') and reorientation periods ('tumbles' or 'traps'). When there are no obstacles present, the mean run duration is much longer than the mean tumble duration, and ensemble averages in the unconfined region follow those expected from the classical run-and-tumble model. In highly confined media, runs are shortened by collisions and tumbles prolonged as cells become 'trapped' within tight or tortuous spots, leading to hop-and-trap dynamics. We demonstrate a smooth transition between run-and-tumble and hop-and-trap behavior through the variation of two motility parameters: *tumble frequency*, the average rate of tumbles initiated, and *tumble failure probability*, the likelihood that the reorientation at the end of a tumble does not allow a cell to move forward (i.e., transition into a 'run' or a 'hop'). We provide context for how quantifiable environmental constraints – confinement and disorder – impact these parameters and shape bacterial motility. Therefore, our work presents a novel framework to characterize the spectrum of bacterial behavior tuned by the interactions between cells and their environments.

Results

A microfluidic system to investigate bacterial motility in structured environments

We construct a microfluidic device to investigate how modulating environmental structure affects swimming behavior in *E. coli*. The device comprises twelve confined regions and one unconfined region, each of size 400 μm x 400 μm. Confined regions contain pillars of 5 μm in height and 10 μm in diameter in varying arrangements (Fig. 1a, 1b); the unconfined region contains no pillars.

Natural environments pose challenges for motile organisms because they can be both physically constraining and heterogeneous. Our device quantifies these challenges using two parameters: *confinement*, a measure of the density of obstacles in a region, and *disorder*, the level of deviation from a perfect grid. Three levels of confinement C are considered: $C = 6$ μm, 2.6 μm, and 1.3 μm. These pillar spacings serve to model the constraint imposed by a range of bacterial habitats, such as soils, sediments, and biological fluids [16, 17, 18]. The chosen values range from the length of a flagellar filament ($\sim 7\mu$m) at the lowest level of confinement to the length of the cell body ($\sim 2\mu$m) at the highest [19, 20]. For levels of disorder D, the center of each pillar is shifted away from the grid position by a value sampled from a uniform distribution with range $[-\frac{DC}{2}, \frac{DC}{2}]$; $D = 0$ corresponds to a perfect grid arrangement (Fig. 1a). For example, for $C = 6$ μm, $D = 0$ region, pillars are horizontally and vertically spaced 6 μm apart (Fig. 1b), whereas for $C = 1.3$ μm, $D = 3$, pillars are initially spaced 1.3 μm apart and their positions are displaced by $(dx, dy) \in$ [-$\frac{3.9}{2}$ μm, $\frac{3.9}{2}$ μm]. Fluorescently labeled *E. coli* in a nutrient-rich medium are flowed into the device for observation (Supplementary Movies 1-3).

Each trial records bacterial movement for forty seconds at a time resolution of 0.05 s. Randomly sampled bacterial trajectories from three structured conditions and in unconfined environments are shown in Fig. 1c ($n = 20$ trajectories from each region). We find that bacteria spend more time in confined regions than in the unconfined region ($\bar{t}_{\text{total}} = 20.1$ s for $n = 110$ trajectories in unconfined v.s. $\bar{t}_{\text{total}} = 22.5$ s for $n = 3991$ trajectories in confined environments, $p < 0.05$). Further, we observe qualitative

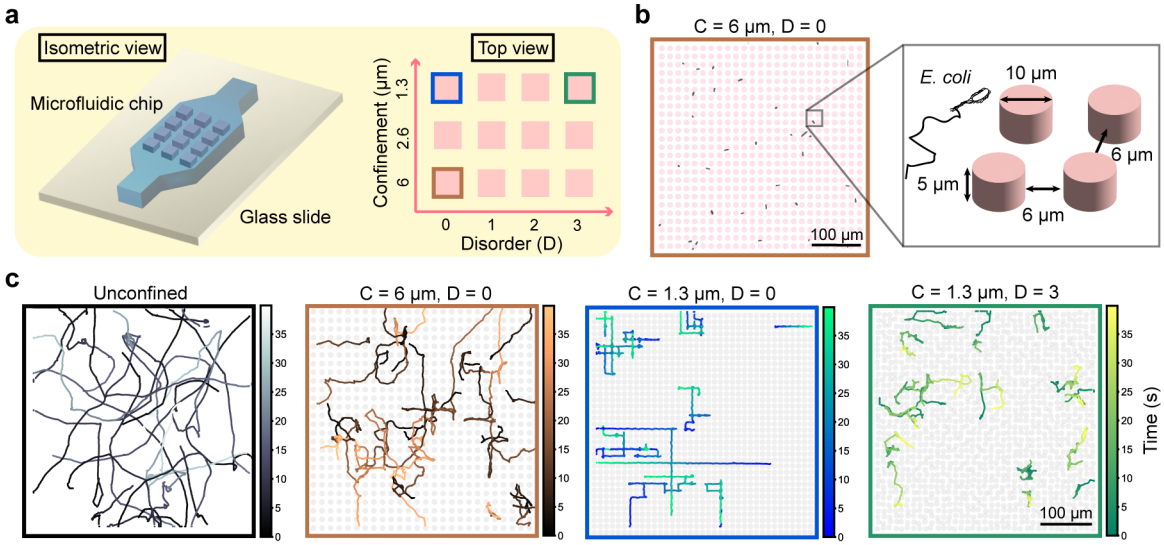

Figure 1. A microfluidic device exposing bacteria to environments of varying levels of confinement and disorder. a Schematic of our experimental device in isometric and top views. The PDMS microfluidic chip comprises twelve regions, represented as pink rectangles. Each region presents a different level of confinement C and disorder D. **b** An example environment with $C = 6$ μm, $D = 0$. Inset shows a schematic of pillar spacing with respect to a swimming *E. coli* cell. **c** Representative tracked trajectories for unconfined and three structured regions (boxed in corresponding colors in **a**). Twenty randomly selected trajectories are shown for each region; color gradient along the track indicates time lapse (darker to lighter coloring from start to end of the trajectory). Cells are tracked using ImageJ plugin 'TrackMate'. All regions are of size 400μm x 400μm; the unconfined region has no pillars.

differences in bacterial trajectories in structured environments and unconfined media (Fig. 1c). For instance, trajectories tend to be directed vertically or horizontally in confined, ordered regions, indicating that bacteria move along rows and columns of pillars rather than performing a uniform exploration of the space as in unconfined environments. Accordingly, we find that trajectories become more tortuous as disorder increases (Fig. 1c, 1d, and Supplementary Fig. 1). In the following sections, we quantitatively analyze these observations.

Run length decreases and tumble bias increases with confinement

We quantify the behavior of individual bacteria by tracking their centers of mass within each region of our microfluidic device. Swimming speeds in the unconfined region, $v\,(t) = |\vec{\mathbf{v}}(t)| \equiv |\vec{\mathbf{r}}\,(t+\delta t) - \vec{\mathbf{r}}\,(t)|\,/\delta t$, are narrowly distributed with mean speed $\langle v \rangle = 24.8$ μm/s, consistent with previously reported *E. coli* swimming speeds of 20-30 μm/s [2, 21], while turn angles, $\delta\theta(t) \equiv \tan^{-1}[\vec{\mathbf{v}}\,(t) \times \vec{\mathbf{v}}\,(t+\delta t)\,/\vec{\mathbf{v}}\,(t) \cdot \vec{\mathbf{v}}\,(t+\delta t)]$, are broadly distributed from 0 to π (Fig. 2a).

In unconfined environments, *E. coli* swim adopting 'run-and-tumble' motility [1, 2]. Runs are defined as intervals during which a cell exhibits smooth forward swimming; here, we denote a 'run' when a cell is swimming at least half the mean unconfined speed, $|\vec{\mathbf{v}}(t)| \geq 12.4$ μm/s, and its turn angle is less than or equal to $\pi/3$ radians (60°). 'Tumbles' are defined as periods when a cell moves slower than half of the mean unconfined speed; turn angles for tumble periods are broadly distributed [3]. We use these definitions across conditions, noting that behavioral states are differentiated similarly in the hop-and-trap model. Hops are like runs, with periods of directed movement with $\delta\theta$ sharply distributed around 0, while traps are like tumbles, showing little forward movement and a wide distribution of turn angles [3]. Speed and angle thresholds are shown in Fig. 2a; selected values limit the trajectory points in the undefined region ($|\vec{v}| > 12.4\mu$m/s, $\delta\theta > \pi/3$) to less than 5%. Our results are not sensitive to the specific value of these thresholds (Supplementary Fig. 2).

Representative trajectories labeled according to these two states (run and tumble) are shown in Fig. 2b. We observe that cells run and tumble alternatively, with runs lasting longer and covering longer distance than tumbles. An example timecourse of speed (labeled in black) and turn angle (labeled in gray) in unconfined regions is shown in Fig. 2c to clearly demonstrate the characteristic features of each

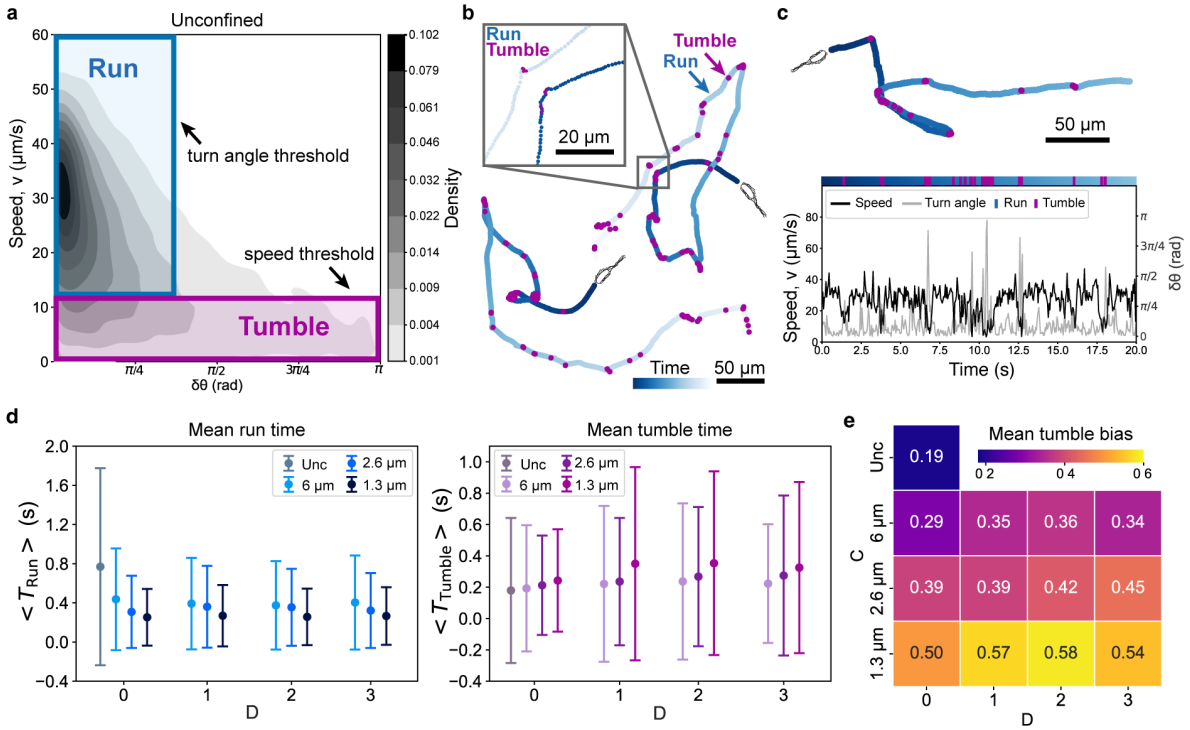

Figure 2: Classification of bacterial trajectories. **a** The bivariate kernel density estimate shows the distributions of bacterial speeds v and turn angles $\delta\theta$ in the unconfined region. Runs (boxed in blue) occur when $v > 12.4$ μm/s (half the mean speed) and $\delta\theta < 3\pi$ rad. Tumbles (boxed in purple) occur when the $v < 12.4$ μm/s. **b** Two sample trajectories from bacteria in the unconfined region, with runs and tumbles colored in blue and purple, respectively. **c** Twenty seconds of a sample trajectory in the unconfined region. Speed (black) and turn angle (grey) values for each frame determine the behavioral state ('run' or 'tumble') assigned to each frame. Color bar above shows discrete sequence of states, with frames assigned as runs shown in blue and tumbles in purple. The label 'unc' represents the unconfined region. **d** Mean run times (left) and mean tumble times (right) for different experimental conditions. **e** Tumble bias across values of confinement C and disorder D.

discrete behavioral state: a run occurs as speed increases and angle drops down close to zero while a tumble occurs as the speed decreases and the angle spikes up.

Extending this discrete state mapping to confined regions allows us to quantify if and how the behavior of individual bacteria changes in response to mechanical cues. For each condition, we compute the mean run time $\langle T_{\text{run}} \rangle$ and the mean tumble time $\langle T_{\text{tumble}} \rangle$ of all tracked cells (Fig. 2d). The mean run time is highest in the unconfined region ($\langle T_{\text{run}} \rangle = 0.77$ s) and lowest in the most confined region ($\langle T_{\text{run}} \rangle = 0.25$ s for $C = 1.3$ μm, $D = 0$). In contrast, we find that the level of disorder does not significantly affect $\langle T_{\text{run}} \rangle$. The mean duration of tumbles do not differ significantly across all assayed conditions (Fig. 2d). The variance in tumble times is increased in disordered regions ($D > 0$) (Fig. 2d). Accordingly, we also see a wider distribution of the turning angle in these regions (Supplementary Fig. 3).

The mean tumble bias, defined as $< P_{\text{tumble}} > \equiv \sum_{i=1}^{N} [n_{i\text{tumble}}/(n_{i\text{tumble}} + n_{i\text{run}})]/N$, where $n_{i\text{tumble}}$ and $n_{i\text{run}}$ are the number of frames assigned to tumble or run states of the ith cell, respectively, and N is the total number of tracked bacteria. It is much higher in structured regions as compared to unconfined media (Fig. 2e). This supports the hypothesis that cells tumble more frequently (i.e., show shorter run durations) when they encounter physical obstacles.

However, we observe more dramatic increases in tumble bias with confinement than accounted for by the corresponding decrease in run duration alone. As noted, bacteria in confined and disordered ($D > 0$) exhibit a larger variance in $\langle T_{\text{tumble}} \rangle$, meaning that not only are tumbles observed more frequently in these regions, but they often last longer as well. We hypothesize that these prolonged tumbles comprise multiple consecutive tumbles that cannot be resolved experimentally (Fig. 2d). These can occur, for instance, because several reorientations may be required for bacteria to move past dead ends created by disordered pillar array geometries. Our results indicate that bacterial dynamics in unconfined and

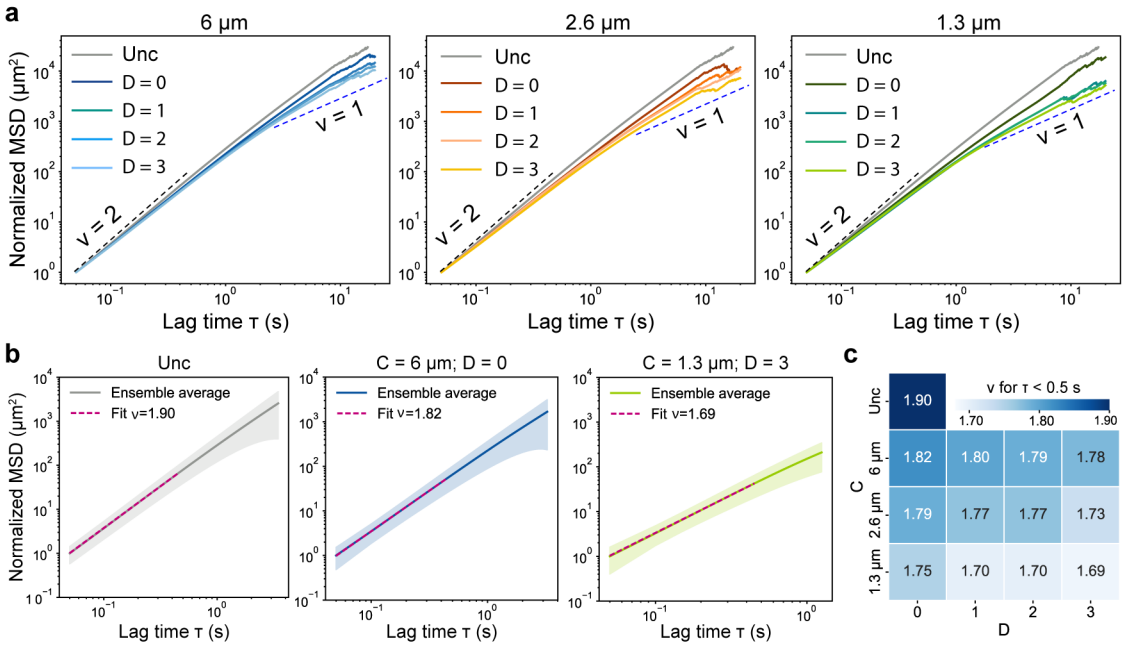

Figure 3. Long-range dynamics across varying levels of confinement and disorder. a Ensemble-averaged mean square displacements (eMSDs) for $C = 6$ μm (left), $C = 2.6$ μm (center), and $C = 1.3$ μm (right). Each plot depicts eMSD curves for varying levels of disorder D. Dashed lines show $\sim t^{\nu}$ for ballistic ($\nu = 2$) and diffusive motion ($\nu = 1$). **b** Curves for eMSDs at early lag times for unconfined (left), $C = 6$ μm; $D = 0$ (center), and $C = 1.3$ μm, $D = 3$ (right). Dashed pink lines show fits estimating ν for $\tau < 0.5$ s. The error bands indicate $\pm$ one standard deviation. **c** Fitted values of ν for $\tau < 0.5$ s across confinement C and disorder D.

confined environments differ largely due to variation in two behavioral parameters: *tumble frequency* (which controls run duration) and *tumble failure probability* (which controls tumble duration).

Characteristic patterns coexist in complex structured environments

A characteristic feature of run-and-tumble motility is that the time- and ensemble-averaged MSD, $eMSD(t) = \left\langle (r(t+\tau) - r(t))^2 \right\rangle$, varies quadratically for short lag times τ and linearly at long lag times above a crossover time τ_c (Fig. 3a). This crossover time corresponds to the mean run duration, that is, $\tau_c = \langle T_{\text{run}} \rangle$. As such, if the only change in motility in structured environments were a shortened run duration, eMSDs would exhibit the same transition from ballistic ($\nu = 2$) to diffusive ($\nu = 1$) behavior with a smaller τ_c. Instead, hop-and-trap dynamics show eMSDs with superdiffusive behavior ($\nu \approx 1.5$) at short lag times with no observed ballistic region. Furthermore, while behavior at long time scales is diffusive ($\nu = 1$) as expected, bacteria in highly confined environments show transiently subdiffusive ($0 < \nu < 1$) motion at intermediate lag times [3].

We find superdiffusive dynamics with $1.5 < \nu < 2$ at short time lags ($0 < \tau < 0.5$ s) in all structured regions considered (Fig. 3b,c), which is in between what might be expected from run-and-tumble and hop-and-trap models. Close examination of individual MSDs indicates that trajectories displaying run-and-tumble and hop-and-trap dynamics are both present in structured regions (Supplementary Fig. 3). Ensemble dynamics display a gradual shift from near-ballistic motion to superdiffusive behavior at small lag times in both highly confined, ordered regions and less confined, highly disordered. For example, $\nu = 1.90$ for unconfined motility as compared to $\nu = 1.75$ for $C = 1.3$ μm, $D = 0$ and $\nu = 1.78$ for $C = 6$ μm, $D = 3$. Regions that are both highly confined and highly disordered skew the closest to hop-and-trap behavior ($\nu = 1.69$ for $C = 1.3$ μm, $D = 3$).

At intermediate lag times, we similarly observe that the proportion of trajectories displaying subdiffusive behavior – characteristic of hop-and-trap dynamics – increases with both confinement and disorder (Supplementary Figs. 4 and 5). However, this trend is weaker in ensemble averages. We note that ensemble-averaged values of ν remain close to 1 until packing is very dense in 3D porous media [3]. As

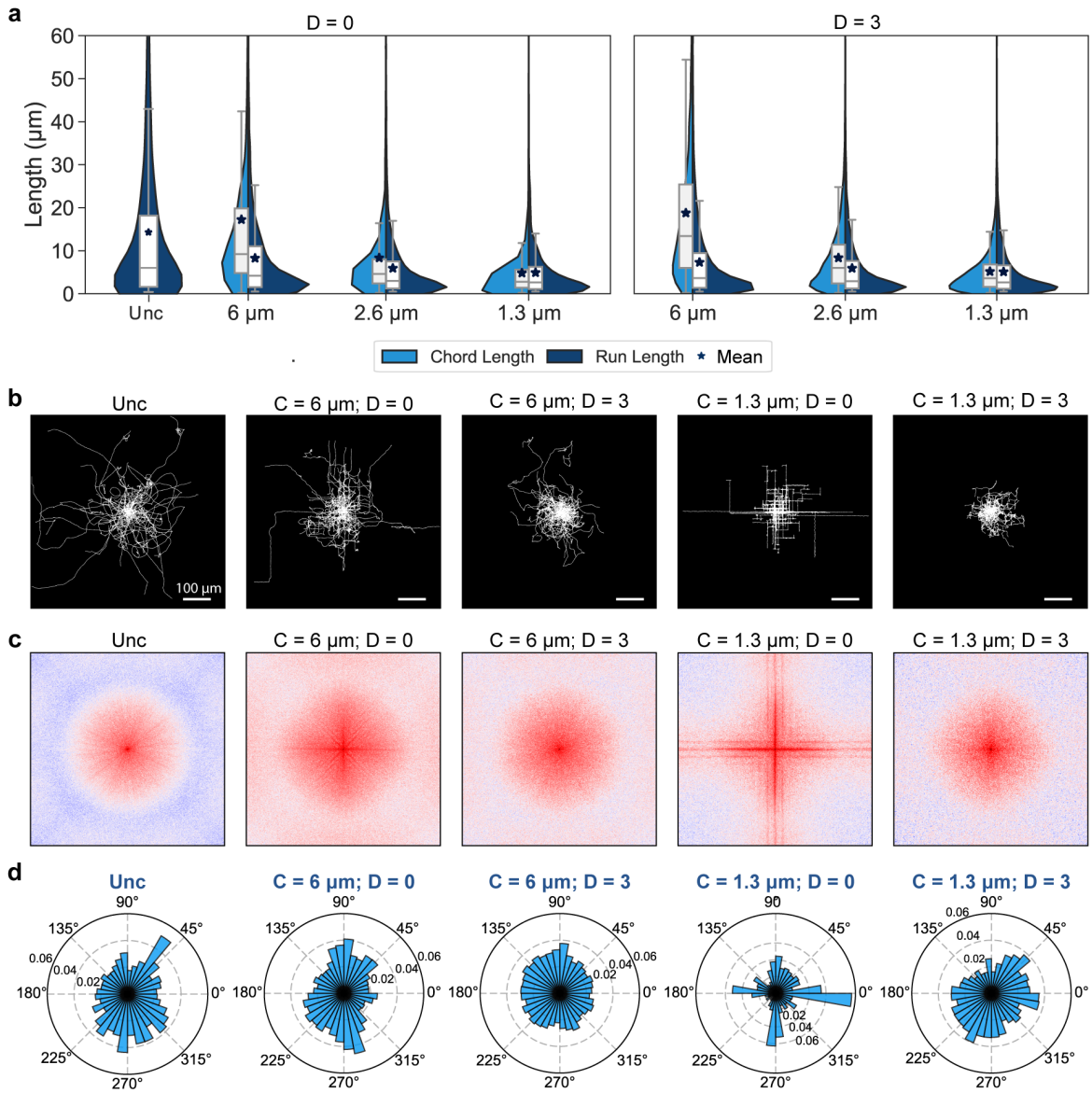

Figure 4. Pillar array geometry is the primary determinant of both duration and direction of swimming. **a** Chord and run length distributions for values of confinement for $D = 0$ (left) and $D = 3$ (right). Box plots mark the lower quartile, median, and upper quartile of the distributions. Mean values are denoted by stars. **b** Re-centered trajectories at (0,0) for selected regions. Each region has 60 trajectories in the sub-plot with the same scale bar (100 μm). **c** Magnitude spectra of FFTs for the corresponding 2D images in **b**. **d** Polar histograms of global turning angle. The global turning angles describes the angle α with respect to the center (0,0) in the fixed coordinate system.

such, this can easily be masked in more intermediate levels of confinement where both run-and-tumble and hop-and-trap dynamics are present. Further, given the quasi-2D nature of our setup and the relative sparsity of our pillar spacing (even in the most confined region tested), we do not expect to fully capture these dynamics at the ensemble level.

Pillar array geometry shapes both duration and direction of swimming

Hop-and-trap behavior is characteristic in highly confined environments; as a result, another hallmark of this locomotive mode is that pore geometry is the primary determinant of hop length and direction [3]. We compute the distribution of straight, possible allowed paths (chords) within each of our pillar array

geometries (Fig. 4a; Supplementary Fig. 6) [22, 23]. Consistent with our previous observations that ensemble behavior aligns with the hop-and-trap model only in the environments with the highest level of confinement, we find that chord length distributions mirror run length distributions only for $C = 1.3$ μm (Fig. 4a). Our results are insensitive to the numbers of chords simulated (Supplementary Fig. 7).

What constrains the distribution of run lengths in intermediate regimes of confinement beyond pore geometry? First, bacteria swim at slower speeds in confinement (averaged run speed of 27.0 μm/s for confined regions vs 29.0 μm/s for unconfined, $p < 0.001$; Supplementary Fig. 2) which means that cells travel shorter distance within a fixed run duration. Previous work found that bacteria in cluttered arenas experience both steric and short-range ($\sim$1-2 μm) interactions with obstacles [24]. Therefore, our calculations likely overestimate the paths available to bacteria in low to medium confinement.

Long-range spatial patterns are noticeably shaped by the physical structure of the environment, with trajectories clearly showing the influence of pillar geometry. In particular, bacteria in regions with regularly distributed pillars ($D = 0$) swim in paths highly directed by vertical and horizontal corridors (Fig. 1c, 4b). As expected from our comparison of chord and run lengths, these patterns are strengthened with increased confinement. We highlight this trend using both Fast Fourier Transform (FFT) analysis (Fig. 4c) and histograms of the global turning angle $\alpha_i = tan^{-1}[(y_i - y_0)/(x_i - x_0)]$, where i ranges from 1 to the total number of frames (Fig. 4d). Notably, disorder has a far greater impact on global turn angles (Fig. 4d) than on local behaviors (Supplementary Fig. 3), with high disorder disrupting the 'directedness' imposed by tight grid-like arrangement.

A modified run-and-tumble model predicts a continuum of motility patterns tuned by tumble frequency and failure

Our experimental results demonstrate that bacterial motility is not defined by a small set of discrete locomotive modes, but instead exists along a continuum with run-and-tumble and hop-and-trap dynamics sitting at opposite extremes. What environmental (or behavioral) factors influence the shift along this continuum between the characteristic signatures of these models? Environmental structure has two major impacts on bacterial motility. First, runs are shortened as cells collide with obstacles. Second, tumbles are lengthened due to cells becoming 'trapped' by tight, tortuous pore spaces (Fig. 5). Accordingly, we hypothesize that the two features that distinguish hop-and-trap dynamics from those expected of the run-and-tumble model – (1) the lack of an observable ballistic region at short lag times and (2) the appearance of transient subdiffusive motion at intermediate lag times before long-timescale diffusive behavior takes hold (Fig. 5a) – appear as run (or 'hop') and tumble (or 'trap') durations are tuned appropriately.

To investigate the role of tumble frequency and failure in shaping the MSD, we conduct a series of numerical simulations. In the 'classic' run-and-tumble model with collisions, tumble failure is not accounted for [24, 25, 26]. As such, tumble duration remains constant and the only observed change is that runs are shortened as tumble frequency (T_{freq}, the average number of tumbles per second) increases due to interactions with obstacles (Supplementary Fig. 11, top left panel). At low tumble frequencies, runs are far longer than tumbles, as expected in unconfined media without obstacles (Fig. 2d, Supplementary Fig. 12). As tumble frequency increases, the ratio of run to tumble duration decreases as runs become shorter (Supplementary Fig. 12). This results in a shorter period of ballistic behavior as the crossover time to diffusive behavior is lowered. At very high tumble frequencies, runs may be so short that the ballistic region cannot be experimentally resolved and superdiffusive dynamics are observed at short time lags (Supplementary Fig. 11, top left panel). Our simulations are performed at $dt = 0.05$ s, equivalent to the time resolution of our experiments; at $T_{\text{freq}} = 8.0$, $\langle T_{\text{run}} \rangle = 0.12$ s ($\sim 2dt$, see Supplementary Fig. 12, upper right panel) in agreement with hop lengths observed in highly confined environments [3, 4].

The other signature of hop-and-trap dynamics, subdiffusive behavior at intermediate time lags, is absent even at very high tumble frequencies with no tumble failure (Supplementary Figs. 10-11). Transient subdiffusion has been observed in systems with long trapping periods within heterogeneous environments [27, 28, 29, 30]; in bacterial systems, we might expect such subdiffusive behavior as prolonged tumbles comprising multiple failed reorientations are observed (see, e.g., Fig. 2d). When $T_{\text{fail}} = 0$, the mean tumble duration does not significantly surpass the mean run duration even at the highest tumble frequency considered (Supplmentary Fig. 12, first row). A tumble can 'fail' in two situations: (1) tight spacing forces the flagellar bundle to stay together, suppressing reorientation (high confinement) or (2) a reorientation cannot initiate a run because of an immediate collision with another obstacle within a 'dead end' cluster (high disorder). Within the context of the run-and-tumble model, a trap can be thought of as a series of 'failed' tumbles (Fig. 5d).

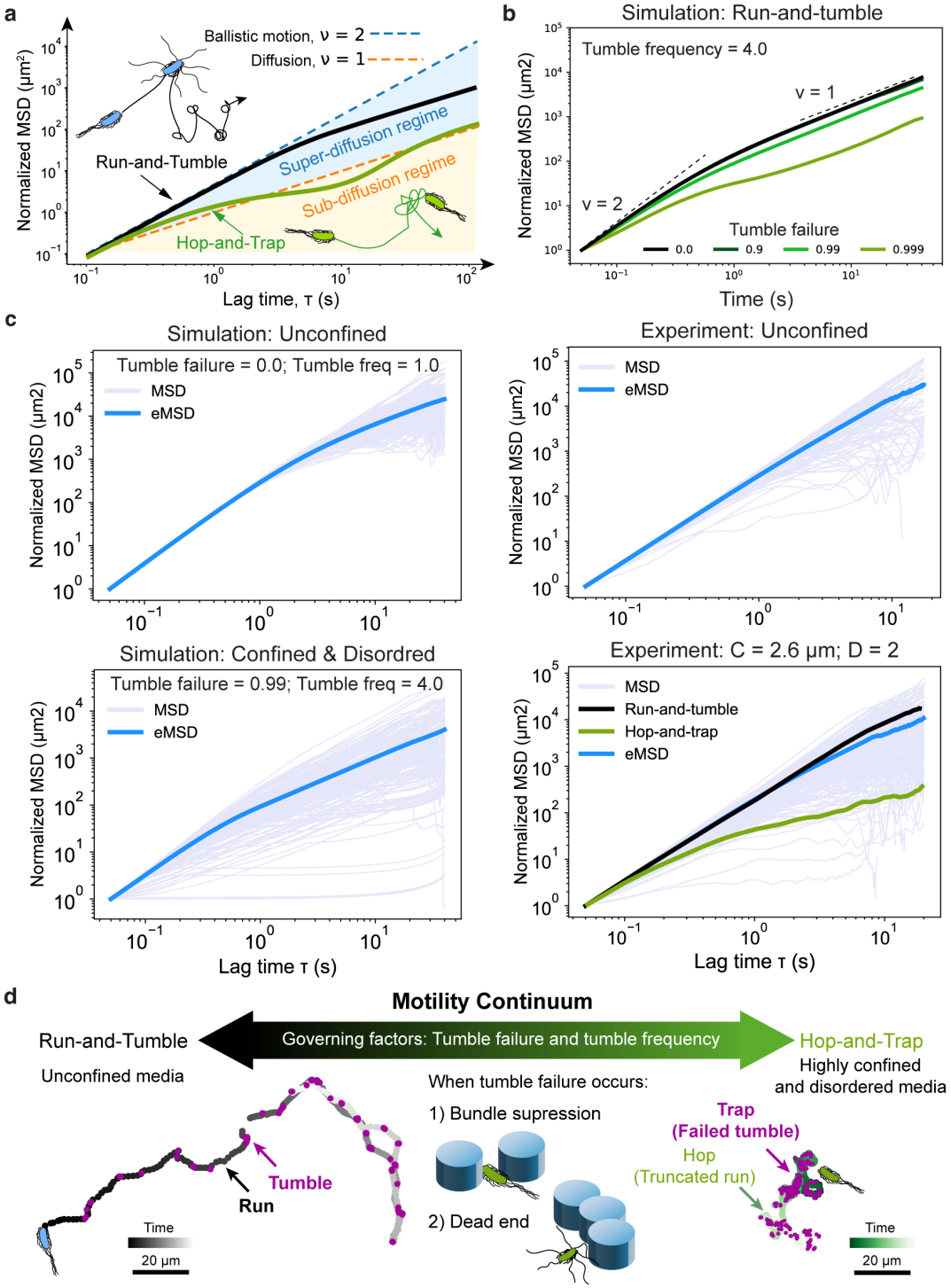

Figure 5. Both experiment and simulation show a continuum of bacterial motility patterns. **a** Schematic of characteristic MSD curves for behavior under run-and-tumble and hop-and-trap models. **b** Normalized ensemble-averaged MSD plot of ensemble dynamics with $T_{\text{freq}} = 0$ and varying tumble failure, T_{fail}. **c** Time-averaged MSDs (in lavender) and ensemble-averaged MSDs (in blue) from simulations and experiments. Simulation parameters are chosen according to those observed in the unconfined region, $T_{\text{fail}} = 0.0$ and $T_{\text{freq}} = 1.0$ (top left), and in a confined and disordered region, $T_{\text{fail}} = 0.99$ and $T_{\text{freq}} = 4.0$ (bottom left). Results are shown from the corresponding experiments in the unconfined region (top right) and C = 2.6 μm, D = 2 (bottom right), respectively. **d** Schematic depicting a continuum of bacterial motility patterns with varying run-and-tumble parameters. Two highlighted trajectories are typical of run-and-tumble and hop-and-trap models corresponding to MSD curves in **c** with C = 2.6 μm; D = 2.

Taking this into consideration, we incorporate the possibility that tumbles can fail and result in a subsequent run of duration 0.0 s. Accordingly, we tune two parameters to simulate motility dynamics: *tumble frequency* (T_{freq}, which modulates the run duration) and *tumble failure probability* (T_{fail}, which modulates the tumble duration). As T_{fail} increases, we observe a smooth increase in the proportion of individual trajectories that display subdiffusive behavior as more cells undergo prolonged tumble (or 'trap') periods (Fig. 5c, left column; Supplementary Fig. 10). This is in agreement with our experiments, in which we observe an increase in the variance of individual MSDs with both confinement and disorder due to an increase in the number of trajectories exhibiting behaviors expected from the hop-and-trap model (Fig. 5c, right column; Supplementary Fig. 4). However, transient subdiffusion at the ensemble level appears only at extremely high T_{fail} (Fig. 5b; Supplementary Fig. 12). This supports the absence of ensemble-level subdiffusive behavior in our experiments (Fig. 3), and aligns with findings that transient subdiffusion emerges only when trap durations significantly exceed hop durations [3]. Overall, this proposed continuum of motility patterns reproduces our experimental results as well as prior experiments in more extreme conditions (Fig. 5).

Discussion

In unconfined environments, peritrichously flagellated bacteria like *E. coli* swim via run-and-tumble motility, in which periods of directed movement (runs) are punctuated by short reorientations (tumbles) [31, 32, 33, 34, 35]. Natural environments, which are often cluttered and heterogeneous, can interfere with this process in two ways. First, runs can be truncated due to collisions with obstacles. Second, tumbles can be extended if a cell is trapped within a tight spot. Accordingly, bacteria in tightly-packed porous media are stuck in place for long bouts of time and are only occasionally able to perform short 'hops' in between subsequent 'traps', a dramatic restructuring of the run-and-tumble model [3, 36]. However, bacterial habitats run the gamut between free solution and highly confined porous gels. Here, we present an experimental framework to systematically characterize the impact of varying environmental confinement (a measure of obstacle density) and disorder (a measure of obstacle randomness) on bacterial motility patterns.

We find that bacterial trajectories displaying run-and-tumble and hop-and-trap dynamics coexist in all structured regions considered, with ensemble dynamics smoothly transitioning between characteristic patterns with increasing confinement and disorder. Our results suggest that bacterial motility lies along a continuum, with run-and-tumble and hop-and-trap dynamics representing the two extremes rather than discrete locomotive modes. We hypothesize that transitions along this continuum are smooth, modulated by parameters that control the duration of runs and tumbles: tumble frequency and tumble failure, respectively. Our modified run-and-tumble model demonstrates that characteristic features of hop-and-trap motility emerge naturally from run-and-tumble behavior as constraints corresponding to confined and disordered environments are imposed.

First, we find that the period of ballistic behavior at short time lags depends primarily on the run duration. As confinement increases, tumbles are initiated at a higher rate due to collisions with obstacles, which leads to truncated run periods. At very high tumble frequencies, runs can be sufficiently shortened so that ballistic behavior is no longer able to be resolved in experiments, giving way to the short timescale superdiffusive dynamics characteristic of hop-and-trap motility (Fig. 5). Second, we find that transient subdiffusion depends on the tumble duration. Tumbles can 'fail' with both increased confinement and disorder, through different mechanisms: in high confinement, flagellar unbundling required for reorientation of the cell body can be suppressed, while in high disorder, cells can be trapped in 'dead ends' created by clutter. Our simulations indicate that subdiffusive behavior in individual trajectories is masked at the ensemble level at all but very high tumble failure probability (Fig. 5); we do not observe subdiffusion in ensemble averages at even our highest confinement level when hop-and-trap dynamics are most dominant (Fig. 3b; Supplementary Fig. 5). This is in accordance with our hypothesis that hop-and-trap behavior sits at an extreme of the spectrum of bacterial motility patterns.

Historically, the mapping between flagella orientation (bundled vs. unbundled) and bacterial motility state (run vs. tumble) emerged under the context of unconfined examination. Our observations shed light on how this mapping breaks down in heterogeneous environments. Particularly, these results elucidate the nuanced structure of motility patterns in peritrichously flagellated bacteria like *E. coli* when taken in the context of natural environments. Cells must navigate a wide array of complex and dynamic terrain; as such, our experimental framework aims to bridge the gap between the more well-studied extremes of free solution and highly-confined media. By capturing the transitions between extreme motility patterns, our work presents a new perspective on bacterial motility as a continuum controlled by a few quantifiable

behavioral and environmental parameters. These results complement the growing literature showing how cell density – a dynamic form of habitat confinement and disorder – acts as its own axis for shifting modes of locomotion [34]. Our work underscores the importance of considering the interactions between cells and their environment, and highlights the need for more comprehensive models to capture the full range of motility strategies employed by bacteria in nature.

Methods

Strains and growth conditions

We grow a culture of wild-type *E. coli* (HCB33) with plasmids expressing red (mScarlet-I) fluorescent proteins on solid LB agar plates (LB Broth EZMix, Sigma-Aldrich + 1.5% Bacto Agar, MOLAR Chemicals). A single colony is subsequently inoculated in 3 mL LB medium (LB Broth EZMix, Sigma-Aldrich) with 50 μg/mL Ampicillin and Streptomycin for 16 h $\pm$ 30 min at 30 C° and 250 rpm. Overnight cultures are back-diluted 1:10,000 in the same medium; this culture has an OD600 of 0.5. 10 μL of this culture is gently mixed with 990 μL of fresh LB medium and antibiotics.

Microfluidic device fabrication and preparation

We design the pillar device using Klayout. We perform a direct write of the pillar device design on a 12.7-cm Cr mask plate (Heidelberg Mask Writer, DWL2000). We subsequently develop the patterns (Hamatech Mask Chrome Etch 1) and then place the mask plate for 2x10 minutes in a hot strip bath.

We prime a new Si wafer by spin coating (3000 rpm/1000 rps/30 s) a thin layer of MicroPrime MP-P20 (ShinEtsu MicroSi, Inc.) to promote adhesion for photoresist. Next, we spin coat Shipley 1813 photoresist on the wafer (using the same protocol) and immediately place it onto a 115 C° hotplate for 60 s. We perform surface analysis (Filmetrics) to check for surface irregularities. The outer ($\sim$1 cm) of photoresist is removed from the edge of the wafer with an Edge Bead Removal System. Using ABM's High Resolution Mask Aligner, we expose the wafer for 3s with Near-UV (405 nm) through our developed mask. The wafer was subsequently developed using MIF 726 (Hamatech-Steag wafer processor). After inspecting the wafer under a microscope, we subject it to a cycle of plasma descum to remove residual layers of photoresist (Anatech Resist Strip). We perform a Bosch fluorine process (Unaxis 770 Deep Silicon Etcher) to achieve a final etch depth of 5 μm, confirmed using the P-7 profilometer. We then strip the wafer of all resist using 2x10 minute wet bath soaks. Finally, we use the MVD-100 molecular vapor deposition system with the anti-stiction coating, 1H,1H,2H,2H-perfluorooctyltrichlorosilane (FOTS).

At this point, the wafer is ready to be used as a master mold of the pillar device. To make the microfluidic chips used for experiments, we mix polydimethylsiloxane (PDMS, Sylgard 184 Silicone Elastomer Kit, Dow Corning) in a ratio of 1:10, degas it in a desiccator, and pour it onto the master mold. We then bake it at 60 C° for 2 h. Devices were cut out from the wafer and we hole-punch 1.5mm-diameter holes at both inlets before binding them to a glass cover slip using an oxygen plasma oven.

Microfluidic experiments and imaging

We wet the device using LB medium with antibiotics immediately after the post-bake upon plasma binding the device to a clean glass bottom Petri-dish. We then inoculate 1 μL of the OD600 = 0.005 suspension in one inlet using a pipette tip. After inoculation, we seal both inlets using High-Vacuum Grease (Dow Corning). The sealed device is then submerged in Milli-Q water (preheated to 30 C°) to prevent the device from drying out and placed onto the microscope stage for imaging. We wait for $\sim$2 h until the main arena of the device reaches sufficient cell density (10-50 cells in the field of view). During the time-lapse microscopy experiment, the temperature of the environment is maintained at 30 C°.

Recording and quantifying bacterial motion

Each device contain 3 levels of confinement for pillar regions and 4 levels of disorder for each level of confinement, amounting to a total of 12 unique pillar regions. Using a Nikon Eclipse Ti-E microscope equipped with a 20x Plan Fluor objective, mCherry fluorescence (49008, Chroma Inc.), and an Andor Neo sCMOS camera (Andor Technology plc.), we took video recordings for 40s (20 fps, 800 frames) at 12 regions with varying arrangements of pillars and one unconfined region without pillars. We repeat the process for a total of 7 times over the course of $\sim$30 minutes to ensure sufficient cell trajectories.

We track between 68 and 605 cells for each region. To trace individual cells, we utilize the ImageJ plugin 'TrackMate' with sub-pixel precision [37]. All tracks are inspected for quality control, and repetitive tracks, tracks that are not shown any sign of motion, and tracks appearing at the boundaries are removed. Raw tracking data (x, y, t) is exported from ImageJ, and further processing and analysis is performed using Python scripts. All scripts and protocols used for analysis are available on Github. All raw images used for this research is publicly accessible in Dropbox.

Starting from the raw tracking data, we assign each frame of a trajectory to a 'run' or 'tumble' state based on a combination of speed and turning angle thresholds. Speed is calculated as $v\left(t\right) = |\vec{\mathbf{v}}(t)| \equiv |\vec{\mathbf{r}}\left(t+\delta t\right) - \vec{\mathbf{r}}\left(t\right)| / \delta t$ and turning angle is defined as $\delta\theta(t) \equiv \tan^{-1}[\vec{\mathbf{v}}\left(t\right) \times \vec{\mathbf{v}}\left(t+\delta t\right) / \vec{\mathbf{v}}\left(t\right) \cdot \vec{\mathbf{v}}\left(t+\delta t\right)]$. We assign a frame as a run state when $v(t) \geq 12.4$ μm/s (half the unconfined mean speed) and $\delta\theta(t) \leq \pi/3$ (i.e., 60°). To identify tumble states, we choose the speed cutoff at half mean speed so cells tumble at times when $v(t) \leq 12.4$ μm/s.

Chord length calculation

We use an in-house Python script to simulate chord lengths in all pillar regions (Supplementary Fig. 6). Chord lengths are defined as randomly sampled, simulated straight paths from randomly positioned origins to the first intersecting pillar. To simulate chord lengths in each region, we recreate pillar arrangements for different levels of confinement and disorder. We then choose 100 randomly located origins from which 100 chords start; each chord ends at the first intersection with a pillar or edge of the device. A probability density is estimated for each region using the Python package Seaborn [38]. Chord length distributions are not sensitive to the number of origins and the number of chords simulated.

Mean-square displacement (MSD) calculation

To compute mean-square displacements (MSDs), we divide tracks into non-overlapping time segments (dt = 0.05 s, corresponding to one frame) as $MSD(\tau) = \left\langle \left(r\left(t+\tau\right) - r\left(t\right)\right)^2 \right\rangle$, where τ is the lag time. The range of τ is chosen to ensure that the minimum number of trajectories is at least 50, with a maximum τ of 20 seconds. The ensemble-averaged MSDs (eMSDs) take the average over bacterial trajectories for a given region. All time- and ensemble-averaged MSDs are shown in Supplementary Figs. 4 and 5, respectively. To fit eMSDs at early lag times ($\tau < 0.5$ s), we use a power law, $y = \beta x^{\alpha}$ where β and the exponent α are two parameters to adjust so as to produce the best fit, using the Python package Scipy [39]. We present a heatmap to show hoe the exponent α varies across conditions.

FFT analysis and global turning angle calculation

Trajectories are centered at the origin by subtracting the first position from all (x, y) positions, $(x', y') = (x - x_0, y - y_0)$. Images are binarized to compute the 2-D discrete Fast Fourier Transform (FFT) using *fft2* function in *Numpy* [40] and plot the FFT amplitude spectrum.

Using the centered trajectories, we compute the global turning angle defined as the angle with respect to the origin $\alpha_i = tan^{-1}[(y_i - y_0)/(x_i - x_0)]$, where i ranges from 1 to the total number of frames. To reduce noise, we utilize a sliding window technique of size 5 frames and 80% overlap. In the polar histograms, the binning covers 0 to 2π. The distribution of the averaged α shows a global direction of bacterial trajectories.

Modified run-and-tumble model simulations

We simulate stochastic run and tumble dynamics in two dimensions via an in-house Python script. Tumbles are initiated at a rate T_{freq} per second; each tumble duration is drawn from an exponential distribution with mean $\langle T_{\text{tumble}} \rangle = 0.2$s (Fig. 2d). Tumble initiations are independent at each time point for each simulated bacterium. This results in exponentially-distributed run duration with mean $\langle T_{\text{run}} \rangle = 1/T_{\text{freq}}$. At time points corresponding to the end of a tumble, another tumble is immediately initiated (corresponding to a failed reorientation) with probability T_{fail}. Simulations are performed at our experimental resolution, with $dt = 0.05$s for $n = 200$ bacteria over a 60 second interval. MSDs for simulated trajectories are calculated as for experimental trajectories.

References

[1] Berg, H. C. & Brown, D. A. Chemotaxis in Escherichia coli analysed by Three-dimensional Tracking. *Nature* **239**, 500–504 (1972).

[2] Berg, H. C. (ed.) *E. coli in Motion.* Biological and Medical Physics, Biomedical Engineering (Springer, New York, NY, 2004).

[3] Bhattacharjee, T. & Datta, S. S. Bacterial hopping and trapping in porous media. *Nature Communications* **10**, 2075 (2019).

[4] Bhattacharjee, T. & Datta, S. S. Confinement and activity regulate bacterial motion in porous media. *Soft Matter* **15**, 9920–9930 (2019).

[5] Lauffenburger, D., Kennedy, C. R. & Aris, R. Traveling bands of chemotactic bacteria in the context of population growth. *Bulletin of Mathematical Biology* **46**, 19–40 (1984).

[6] Duffy, K. J., Cummings, P. T. & Ford, R. M. Random walk calculations for bacterial migration in porous media. *Biophysical journal* **68**, 800–806 (1995).

[7] Croze, O. A., Ferguson, G. P., Cates, M. E. & Poon, W. C. Migration of chemotactic bacteria in soft agar: role of gel concentration. *Biophysical journal* **101**, 525–534 (2011).

[8] Chaban, B., Hughes, H. V. & Beeby, M. The flagellum in bacterial pathogens: For motility and a whole lot more. *Seminars in Cell & Developmental Biology* **46**, 91–103 (2015).

[9] Zegadło, K. *et al.* Bacterial Motility and Its Role in Skin and Wound Infections. *International Journal of Molecular Sciences* **24**, 1707 (2023).

[10] Keegstra, J. M., Carrara, F. & Stocker, R. The ecological roles of bacterial chemotaxis. *Nature Reviews Microbiology* **20**, 491–504 (2022).

[11] Chepsergon, J. & Moleleki, L. N. Rhizosphere bacterial interactions and impact on plant health. *Current Opinion in Microbiology* **73**, 102297 (2023).

[12] Fenchel, T. Motility of bacteria in sediments. *Aquatic Microbial Ecology* **51**, 23–30 (2008).

[13] Hoshino, T. *et al.* Global diversity of microbial communities in marine sediment. *Proceedings of the National Academy of Sciences* **117**, 27587–27597 (2020).

[14] Wu, C. M. *et al.* Mucin glycans drive oral microbial community composition and function. *npj Biofilms and Microbiomes* **9**, 11 (2023).

[15] Jin, C. & Sengupta, A. Microbes in porous environments: from active interactions to emergent feedback. *Biophysical Reviews* **16**, 173–188 (2024).

[16] Fatin-Rouge, N., Starchev, K. & Buffle, J. Size effects on diffusion processes within agarose gels. *Biophysical journal* **86**, 2710–2719 (2004).

[17] Zalc, J. M., Reyes, S. C. & Iglesia, E. The effects of diffusion mechanism and void structure on transport rates and tortuosity factors in complex porous structures. *Chemical Engineering Science* **59**, 2947–2960 (2004).

[18] Lindquist, W. B., Venkatarangan, A., Dunsmuir, J. & Wong, T.-f. Pore and throat size distributions measured from synchrotron x-ray tomographic images of fontainebleau sandstones. *Journal of Geophysical Research: Solid Earth* **105**, 21509–21527 (2000).

[19] Namba, K., Yamashita, I. & Vonderviszt, F. Structure of the core and central channel of bacterial flagella. *Nature* **342**, 648–654 (1989).

[20] Nirody, J. A., Sun, Y.-R. & Lo, C.-J. The biophysicist's guide to the bacterial flagellar motor. *Advances in Physics: X* **2**, 324–343 (2017).

[21] Chattopadhyay, S., Moldovan, R., Yeung, C. & Wu, X. L. Swimming efficiency of bacterium Escherichia coli. *Proceedings of the National Academy of Sciences* **103**, 13712–13717 (2006).

[22] Dehkharghani, A., Waisbord, N. & Guasto, J. S. Self-transport of swimming bacteria is impaired by porous microstructure. *Communications Physics* **6**, 1–9 (2023).

[23] Levitz, P. & Tchoubar, D. Disordered porous solids : from chord distributions to small angle scattering. *Journal de Physique I* **2**, 771–790 (1992).

[24] Sosa-Hernández, J. E., Santillán, M. & Santana-Solano, J. Motility of escherichia coli in a quasi-two-dimensional porous medium. *Physical Review E* **95**, 032404 (2017).

[25] Licata, N. A., Mohari, B., Fuqua, C. & Setayeshgar, S. Diffusion of Bacterial Cells in Porous Media. *Biophysical Journal* **110**, 247–257 (2016).

[26] Dentz, M., Creppy, A., Douarche, C., Clément, E. & Auradou, H. Dispersion of motile bacteria in a porous medium. *Journal of Fluid Mechanics* **946**, A33 (2022).

[27] Berezhkovskii, A. M., Dagdug, L. & Bezrukov, S. M. Discriminating between anomalous diffusion and transient behavior in microheterogeneous environments. *Biophysical journal* **106**, L09–L11 (2014).

[28] Ernst, M. *et al.* A model for the transient subdiffusive behavior of particles in mucus. *Biophysical journal* **112**, 172–179 (2017).

[29] Yamamoto, E., Akimoto, T., Yasui, M. & Yasuoka, K. Origin of subdiffusion of water molecules on cell membrane surfaces. *Scientific reports* **4**, 4720 (2014).

[30] Saxton, M. J. A biological interpretation of transient anomalous subdiffusion. i. qualitative model. *Biophysical journal* **92**, 1178–1191 (2007).

[31] Turner, L., Ryu, W. S. & Berg, H. C. Real-Time Imaging of Fluorescent Flagellar Filaments. *Journal of Bacteriology* **182**, 2793–2801 (2000).

[32] Xie, L., Altindal, T., Chattopadhyay, S. & Wu, X.-L. Bacterial flagellum as a propeller and as a rudder for efficient chemotaxis. *Proceedings of the National Academy of Sciences* **108**, 2246–2251 (2011).

[33] Tian, M., Wu, Z., Zhang, R. & Yuan, J. A new mode of swimming in singly flagellated Pseudomonas aeruginosa. *Proceedings of the National Academy of Sciences of the United States of America* **119**, e2120508119 (2022).

[34] Wadhwa, N. & Berg, H. C. Bacterial motility: machinery and mechanisms. *Nature Reviews Microbiology* **20**, 161–173 (2022).

[35] Craig, L., Forest, K. T. & Maier, B. Type IV pili: dynamics, biophysics and functional consequences. *Nature Reviews Microbiology* **17**, 429–440 (2019).

[36] Bhattacharjee, T., Amchin, D. B., Ott, J. A., Kratz, F. & Datta, S. S. Chemotactic migration of bacteria in porous media. *Biophysical Journal* **120**, 3483–3497 (2021).

[37] Tinevez, J.-Y. *et al.* Trackmate: An open and extensible platform for single-particle tracking. *Methods* **115**, 80–90 (2017).

[38] Waskom, M. L. seaborn: statistical data visualization. *Journal of Open Source Software* **6**, 3021 (2021).

[39] Virtanen, P. *et al.* SciPy 1.0: Fundamental Algorithms for Scientific Computing in Python. *Nature Methods* **17**, 261–272 (2020).

[40] Harris, C. R. *et al.* Array programming with numpy. *Nature* **585**, 357–362 (2020).

Acknowledgements

H.Z. and J.A.N. acknowledge funding support by NSF-Simons National Institute for Theory and Mathematics in Biology, which is jointly supported by the U.S. National Science Foundation (Award 2235451) and the Simons Foundation (Award MP-TMPS-00005320). H.Z. is also grateful for her graduate program in Biophysical Sciences at the University of Chicago. M.T.W., H.K., C.E.F., and J.A.N. acknowledge support from The Santa Fe Institute and The James S. McDonnell Foundation Postdoctoral Fellowship Award in Complex Systems (M.T.W: `https://doi.org/10.37717/2020-1543`; H.K.: `https://doi.org/10.37717/2021-3524`; C.E.F.: `https://doi.org/10.37717/2020-1591`; J.A.N.: `https://doi.org/10.37717/220020527`). C.E.F. is supported by the NSF-Simons Center for Quantitative Biology at Northwestern University (NSF: 1764421 and Simons Foundation/SFARI 597491-RWC). J.A.N. and E.M.M. acknowledge support from the National Science Foundation through the Center for Living Systems (Grant # 2317138). This work was performed in part at the Cornell NanoScale Facility, a member of the National Nanotechnology Coordinated Infrastructure (NNCI), which is supported by the National Science Foundation (Grant NNCI-2025233). We thank Tom Pennell for his guidance and advice throughout the fabrication process at the Cornell NanoScale Facility. We also thank Benjamin R. Epley, Erin Brandt, Peter J. Yunker and Juan E. Keymer for their insights and many thoughtful discussions.

Author information

Authors and Affiliations

Graduate Program in Biophysical Sciences, University of Chicago, 929 East 57th St, Chicago, IL 60637
Haibei Zhang
School of Applied and Engineering Physics, Cornell University, Clark Hall, 271, 142 Sciences Dr, Ithaca, NY 14853 and **School of Physics, Georgia Institute of Technology, 837 State St NW, Atlanta, GA 30332**
Miles T. Wetherington
Department of Mechanical and Aerospace Engineering, Princeton University, 41 Olden St, Princeton, NJ 08544
Hungtang Ko
Department of Engineering Sciences and Applied Mathematics, Northwestern University, 2145 Sheridan Rd, Evanston, IL 60208
Cody E. FitzGerald
Department of Molecular Genetics and Cell Biology, University of Chicago, 920 E. 58th St, Chicago, IL 60637
Edwin M. Munro
Department of Organismal Biology and Anatomy, University of Chicago, 1027 E 57th St, Chicago, IL 60637
Jasmine A. Nirody

Contributions

M.T.W., H.K., C.E.F., H.Z., and J.A.N. designed the research; M.T.W. performed experiments; H.Z. analyzed the data; J.A.N. performed simulations; H.Z. and J.A.N. wrote the manuscript; H.Z., M.T.W., H.K, C.E.F., E.M.M, and J.A.N. reviewed and edited the manuscript.

Corresponding author

Correspondence to Jasmine A. Nirody
Email: jnirody@uchicago.edu

Ethics declarations

Competing interests

The authors declare no competing interests.